Nuclear forces and their impact on neutron-rich nuclei and neutron-rich matter

K. Hebeler,[1,2] J. D. Holt,[1,2,3] J. Menéndez[1,2,4] and A. Schwenk[1,2]

[1]Institut für Kernphysik, Technische Universität Darmstadt, 64289 Darmstadt, Germany
[2]ExtreMe Matter Institute EMMI, GSI Helmholtzzentrum für Schwerionenforschung GmbH, 64291 Darmstadt, Germany
[3]TRIUMF, 4004 Wesbrook Mall, Vancouver, British Columbia, V6T 2A3 Canada
[4]Department of Physics, University of Tokyo, Hongo, Tokyo 113-0033, Japan
emails: kai.hebeler@physik.tu-darmstadt.de, jholt@triumf.ca, menendez@nt.phys.s.u-tokyo.ac.jp, schwenk@physik.tu-darmstadt.de

Keywords

Abstract

We review the impact of nuclear forces on matter at neutron-rich extremes. Recent results have shown that neutron-rich nuclei become increasingly sensitive to three-nucleon forces, which are at the forefront of theoretical developments based on effective field theories of quantum chromodynamics. This includes the formation of shell structure, the spectroscopy of exotic nuclei, and the location of the neutron dripline. Nuclear forces also constrain the properties of neutron-rich matter, including the neutron skin, the symmetry energy, and the structure of neutron stars. We first review our understanding of three-nucleon forces and show how chiral effective field theory makes unique predictions for many-body forces. Then, we survey results with three-nucleon forces in neutron-rich oxygen and calcium isotopes and neutron-rich matter, which have been explored with a range of many-body methods. Three-nucleon forces therefore provide an exciting link between theoretical, experimental and observational nuclear physics frontiers.

Contents

1. INTRODUCTION

Recent studies have shown that three-nucleon (3N) forces play a key role for understanding and predicting neutron-rich nuclei and for the formation and evolution of shell structure. In addition, the location of the neutron dripline, where nuclei cease to be bound, is sensitive to small interaction contributions and therefore to 3N forces. At the same time, 3N forces are the dominant uncertainty in constraining the properties of neutron-rich matter at nuclear densities, which is important for the structure of neutron stars. This leads to an exciting connection of 3N forces with the exploration of extreme neutron-rich nuclei at rare isotope beam facilities and with forefront observations in astrophysics.

In the following, we discuss our understanding of nuclear forces based on chiral effective field theory (EFT) and show how this framework makes unique predictions for many-body forces. In particular, the properties of all nuclei can be predicted up to high order (next-to-next-to-next-to-leading order, N^3LO), with just two new low-energy couplings in many-body forces. To this order all other three- and four-nucleon (4N) interactions depend on couplings that are determined from interactions with pions or enter in two-nucleon (NN) interactions. We discuss theoretical developments of the subleading 3N forces and advances towards including them in few- and many-body calculations. In Sections 2 and 3, we survey results with 3N forces in neutron-rich oxygen and calcium isotopes, which have been explored with a range of many-body methods. These present key regions in the study of the neutron dripline, of shell structure, and in the spectroscopy of exotic nuclei. In Section 4, we discuss the impact of nuclear forces on the properties of neutron-rich matter, including the neutron skin, the symmetry energy, and the properties of neutron stars. Finally, we conclude and give an outlook with open problems and opportunities in Section 5.
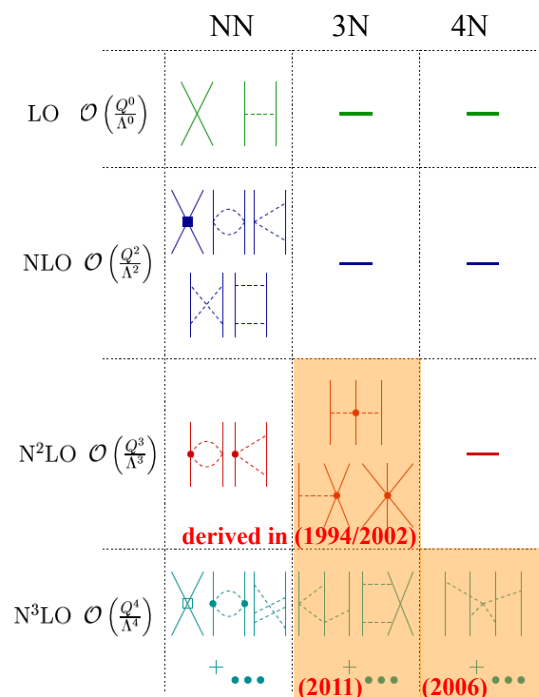
Figure 1

Chiral EFT for nuclear forces, where the different contributions at successive orders are shown diagrammatically [figure adapted from (1, 2)]. Nucleons and pions are represented by solid and dashed lines, respectively. Many-body forces are highlighted in orange including the year they were derived [3N forces at N^2LO (3, 4) and N^3LO (5, 6); 4N forces at N^3LO (7)]. All N^3LO 3N and 4N forces are predicted parameter-free.

1.1. Chiral EFT for nuclear forces

Chiral EFT provides a systematic basis for strong interactions at momentum scales of the order of the pion mass $Q \sim m_\pi$ based on the symmetries of quantum chromodynamics (QCD) (1, 2). In chiral EFT, nucleons interact via pion exchanges and shorter-range contact interactions. The resulting nuclear forces and consistent electroweak operators are organized in a systematic expansion in powers of Q/Λ_b, where $\Lambda_b \sim 500\,\text{MeV}$ denotes the breakdown scale, leading to a typical expansion parameter $Q/\Lambda_b \sim 1/3$. The EFT enables controlled calculations with theoretical error estimates, which is especially important for exotic nuclei and neutron-rich matter under extreme conditions in astrophysics. Moreover, chiral EFT connects nuclear forces to the underlying theory through lattice QCD (8, 9).

Generally, nuclear forces are not observable and depend on a resolution scale Λ, so that the nuclear Hamiltonian is given by $H(\Lambda) = T(\Lambda) + V_{NN}(\Lambda) + V_{3N}(\Lambda) + V_{4N}(\Lambda)\ldots$ As shown in **Figure 1**, at a given order, nuclear forces include contributions from one- or multi-pion exchanges that govern the long- and intermediate-range parts and from short-range contact interactions. For each Λ, the scale-dependent short- range couplings are fit to low-energy data and thus capture all short-range effects relevant at low energies. While 3N forces are not observable, there are natural sizes to many-body-force contributions that

$1/m$

(a)   (b)   (c)   (d)   (e)   (f)   (g)
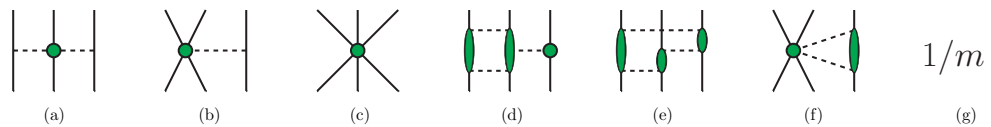
Figure 2

Different topologies that contribute to 3N forces up to N^{3}LO. The shaded vertices denote the amplitudes of the corresponding pion/nucleon interactions. The individual diagrams are: (a) 2π exchange, (b) 1π-contact, (c) 3N contact, (d) 2π-1π exchange, (e) ring contributions, (f) 2π-contact, and (g) relativistic corrections. Figure taken from Reference (16).

are made manifest in the EFT power counting and which explain the phenomenological hierarchy of many-body forces, $V_{\mathrm{NN}}(\Lambda) > V_{\mathrm{3N}}(\Lambda) > V_{\mathrm{4N}}(\Lambda)$ (1, 2). The effects discussed in this review are dominated by the long-range parts of 3N forces and are therefore expected to be robust. Even though it is tempting to neglect contributions from 3N forces in cases when calculations based on only NN forces provide a good description of experimental data [see, e.g., Reference (10)], EFT power counting dictates the inclusion of all many-body forces up to a given order. In fact, explicit calculations show that 3N forces always provide important contributions in nuclei and matter (see Sections 2, 3 and 4). The scale dependence can also be exploited by using the renormalization group (RG) to systematically change the resolution scale, while preserving low-energy observables. This can be advantageous for calculations of nuclei and nucleonic matter, because the evolution to lower scales facilitates the solution of the nuclear many-body problem due to a decoupling of low and high momenta in the Hamiltonian (11, 12).

1.2. Many-body forces

Chiral EFT opens up a systematic path to investigate many-body forces and their impact on few- and many-body systems (13). An important feature of chiral EFT is the consistency of NN and 3N (and higher-body) interactions. This determines the long-range two-pion-exchange parts of 3N forces at next-to-next-to-leading order (N^{2}LO), with pion-nucleon couplings c_1, c_3, c_4, leaving only two low-energy couplings c_D and c_E that encode pion interactions with short-range NN pairs and short-range three-body physics, respectively (3, 4). To fit c_D and c_E, different uncorrelated observables are used, e.g., the binding energy and half life of ^{3}H (14), or the binding energy of ^{3}H and the charge radius of ^{4}He (15).

At the next order, all many-body interactions are predicted parameter-free with many new structures, as shown in **Figure 2**. These also depend on the leading NN contact interactions C_S, C_T (5, 6) [see the 2π-contact contributions (f) and the relativistic corrections (g)]. Interestingly, for systems of only neutrons, the N^{2}LO c_D and c_E parts do not contribute because of the Pauli principle and the coupling of pions to spin (17). Therefore, chiral EFT predicts all three-neutron and four-neutron forces to N^{3}LO.

The leading N^{2}LO 3N forces improve few-body scattering, but interesting open problems remain (18). This makes the application of 3N and 4N forces at the next order (N^{3}LO) very exciting. The derivation of N^{3}LO 3N forces has only been completed recently (5, 6), but no calculation exists for nuclei beyond $A = 3$, where the current state-of-the-art are N^{3}LO NN plus N^{2}LO 3N calculations, or consistent calculations at N^{2}LO (see Sections 2 and 3). The practical calculation of all topologies of Figure 2 in a form suitable for few- and many-body calculations is a nontrivial task. Due to the large amounts of required computational

resources, 3N matrix elements so far have only been available in small basis spaces (19). Recently, a novel and numerically much more efficient method has been developed for decomposing 3N forces in a plane-wave partial-wave basis (16). The new framework makes explicit use of the fact that all unregularized contributions to chiral 3N forces are either local, i.e., they depend only on momentum transfers, or they contain only polynomial non-local terms. These new developments allow to calculate matrix elements of all N^3LO 3N contributions for large basis spaces required for ab initio studies of nuclei and nucleonic matter. An important open problem is to fit all NN and 3N low-energy couplings at N^3LO consistently. To this end, it may be beneficial to fit several different few-body observables simultaneously within theoretical uncertainties, or to include also information beyond few-nucleon systems in the fits. The exploration of these strategies is currently in progress.

2. NEUTRON-RICH OXYGEN ISOTOPES

With a closed $Z = 8$ proton shell, the oxygen isotopes provide an exciting laboratory to study nuclear forces with a range of many-body methods. The oxygen chain also exhibits remarkable aspects of exotic nuclei. In oxygen, the location of the neutron dripline at neutron number $N = 16$ is anomalously close to the stable nuclei [at the same N as for carbon ($Z = 6$) and nitrogen ($Z = 7$)], see Section 2.1. Adding a single proton to oxygen is able to bind six more neutrons to ^{31}F. As discussed in Section 2.2, oxygen features two more shell closures in ^{22}O and ^{24}O, where the latter doubly magic nucleus lies just at the neutron dripline. In recent years, experimental advances have even allowed explorations of oxygen isotopes beyond the dripline to ^{26}O, see Section 2.3.

In the following, we discuss results for the neutron-rich oxygen isotopes and neighboring nuclei based on chiral EFT interactions. In particular, the softening of nuclear forces by RG transformations (11, 12) enabled many new calculations of nuclei with a range of many-body methods. The results with 3N forces surveyed in this review have been mainly performed using two different strategies for the Hamiltonian with different RG approaches. The first uses the RG to evolve NN interactions to low-momentum interactions $V_{\text{low }k}$ (11). At the NN level, the results discussed here start from the 500 MeV N^3LO potential of Reference (20). Chiral 3N forces provide a general low-momentum basis, so that the low-momentum NN interactions have been combined with N^2LO 3N forces fit to the ^{3}H binding energy and the ^{4}He charge radius (15). We will refer to these Hamiltonians as low-momentum NN+3N forces. Note that similar results are obtained if the RG evolution at the NN level is replaced by a similarity RG (SRG) evolution (15). The second strategy for the Hamiltonian uses a SRG transformation applied consistently to chiral NN and 3N interactions (21, 22). The results discussed in this review start from the same NN potential and include the same N^2LO 3N operators, but with local regulators (23), fit to the binding energy and half life of ^{3}H (14). We will refer to these Hamiltonians as SRG-evolved NN+3N-full Hamiltonian, or NN+3N-ind Hamiltonian if the SRG evolution starts only from the NN potential, but induced (ind) 3N interactions are kept. The latter corresponds to the results for the "bare" 500 MeV N^3LO potential, if induced higher-body interactions can be neglected.

Next, we briefly discuss the different ab initio many-body methods used for medium-mass nuclei. These can be grouped into calculations based on valence-space Hamiltonians and calculations obtained directly in large many-body spaces. The latter treat all nucleons as active in a large basis space and rely on different, controlled approximations to solving the many-body problem of A nucleons. For calculations based on valence-space Hamiltonians,

the number of active degrees of freedom is reduced by treating the nucleus as a many-body system comprised of a closed-shell core with the additional A_v valence nucleons occupying a truncated valence space. The valence-space Hamiltonian, which is diagonalized exactly, includes configurations from the large basis space via different many-body methods.

Great advances to access large basis spaces have been made with coupled-cluster (CC) theory (24). The CC method starts from a closed-shell reference state and includes correlations through a similarity transformation $\overline{H} = e^{-T} H e^{T}$, where H is the normal-ordered Hamiltonian. In state-of-the-art calculations the cluster operator $T = T_1 + T_2 + \cdots + T_A$, which generates particle-hole excitations to all orders, is truncated at the singles and doubles (CCSD) level, $T_1 + T_2$, and includes triples excitations, T_3, in a nonperturbative but approximate way. At the CCSD level, T_1 and T_2 are obtained by solving the CC equations, which follow from the reference state having no one-particle–one-hole or two-particle–two-hole excitations. Equations-of-motion CC methods can access ground and excited states of one- or two-particles-attached and one-particle-removed systems from closed-shell nuclei.

A novel ab initio many-body method is the in-medium similarity renormalization group (IM-SRG) (25, 26). The IM-SRG uses a continuous unitary transformation $U(s)$, parameterized by the flow parameter s, to drive the Hamiltonian to a band- or block-diagonal form. This is accomplished by solving the flow equation $\frac{dH(s)}{ds} = [\eta(s), H(s)]$, where $\eta(s) = \frac{dU(s)}{ds} U^{\dagger}(s)$ is the generator of the transformation. With a suitable choice of $\eta(s)$, the off-diagonal part of the Hamiltonian is driven to zero as $s \to \infty$. Similarly to the CC approach, the IM-SRG decouples the closed-shell ground state from the space of particle-hole excitations on top of it. Recently, a multi-reference formulation (MR-IM-SRG) was developed, which enables to describe also ground states of open-shell nuclei (27).

In self-consistent Green's function theory (SCGF) (28), the quantity of interest is the single-particle Green's function, which describes the propagation of single-particle and single-hole excitations in the many-body system. From this the ground-state energy can be calculated via the Koltun sum rule (29). The Gorkov formalism (30, 31) allows to treat pairing correlations explicitly and extends SCGF calculations to open-shell nuclei.

Other calculations of oxygen isotopes in large many-body spaces include the importance-truncation no-core shell-model (IT-NCSM) (32, 33), which extends an exact diagonalization with the NCSM by using importance sampling to access larger spaces, and nuclear lattice simulations (34), which solve the many-body problem of nucleons on a Euclidean space-time lattice. In lattice EFT, the energies of the ground and excited states are obtained by propagating the system in imaginary time, as in lattice QCD.

Approaches based on valence-space Hamiltonians allow the calculation of ground and excited states of all nuclei in the valence space provided that the diagonalization is feasible (35). Many-body perturbation theory (MBPT) (36) has been used to derive valence-space Hamiltonians, based on a diagrammatic approach for calculating the single-particle energies (SPEs) and the interactions between valence nucleons. The MBPT includes the contributions from configurations outside the valence space perturbatively. State-of-the-art MBPT results include NN and 3N forces to third order for the valence-space interactions and the consistent SPEs [see Reference (37) for oxygen isotopes].

Recently, nonperturabtive derivations of valence-space Hamiltonians have been achieved based on the IM-SRG and CC methods. In the IM-SRG for open-shell nuclei, states with A_v particles in the valence space are additionally decoupled from those containing non-valence admixtures (38, 39). This gives the energy of the closed-shell core (as in the standard IM-SRG), but also valence-space SPEs and interactions. In the CC effective interaction (CCEI)
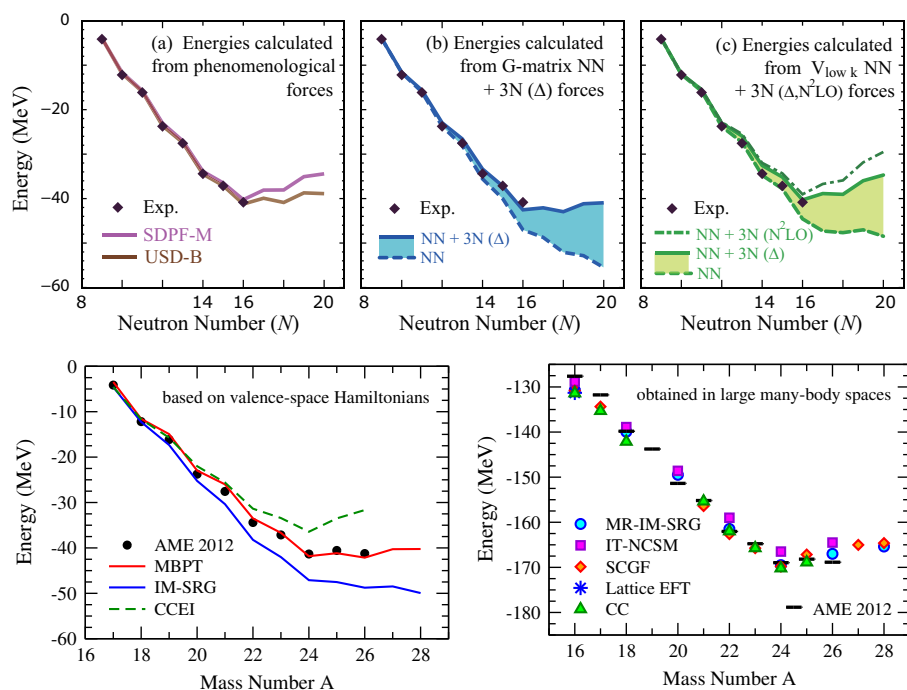
Figure 3

Top panel: Ground-state energies of oxygen isotopes measured from ^{16}O, including experimental values of the bound $^{16-24}$O. Figure taken from (42). Energies obtained from (a) phenomenological forces SDPF-M (43) and USDB (44), (b) a G matrix and including Fujita-Miyazawa 3N forces due to Δ excitations, and (c) from low-momentum interactions $V_{\mathrm{low}\,k}$ and including N^{2}LO 3N forces as well as only due to Δ excitations. The changes due to 3N forces based on Δ excitations are highlighted by the shaded areas. Bottom panels: Left: Ground-state energies of oxygen isotopes relative to ^{16}O based on valence-space Hamiltonians, compared to the atomic mass evaluation (AME 2012) (45). The MBPT results are performed in an extended $sdf_{7/2}p_{3/2}$ valence space (37) based on low-momentum NN+3N forces, while the IM-SRG (39) and CCEI (40) results are in the sd shell from a SRG-evolved NN+3N-full Hamiltonian. Right: Ground-state energies obtained in large many-body spaces: MR-IM-SRG (27), IT-NCSM (27), SCGF (29), CC (40), based on the SRG-evolved NN+3N-full Hamiltonian, and Lattice EFT (34), based on NN+3N forces at N^{2}LO.

approach, a similar decoupling for a given nucleus is achieved using a Lee-Suzuki similarity transformation from the CC solution in the large basis space to the valence space (40, 41).

2.1. Location of the neutron dripline

The neutron drip line evolves regularly from light to medium-mass nuclei except for a striking anomaly in the oxygen isotopes, where the dripline is at a doubly magic nucleus ^{24}O and anomalously close to the stable nuclei. This anomaly is challenging to explain in microscopic theories based only on NN forces that reproduce NN scattering (42). This is illustrated in the top panel of **Figure 3** with sd-shell calculations based on second-order MBPT [dashed lines in panels (b) and (c)], where the ground-state energies decrease up to $N = 20$, leading to an incorrect dripline at ^{28}O. This is in contrast to phenomenological interactions ad-

justed to experiment, shown in panel (a), which have a minimum at ^{24}O because the $d_{3/2}$ orbital remains unbound. The comparison shows that NN forces only lead to too attractive interactions among valence neutrons, which causes the $d_{3/2}$ orbital to become bound in ^{24}O and beyond. These deficiencies have been traced to the monopole components of the valence-space Hamiltonian, as these parts are amplified with neutron number, and it has been argued that 3N forces are important for the monopole components (46). This is also supported by the cutoff dependence of the monopole components with NN forces only (47).

First investigations of neutron-rich oxygen isotopes with 3N forces (42) have shown that 3N forces lead to repulsive interactions between valence neutrons. This is dominated by the long-range parts of 3N forces, as highlighted by the results for Fujita-Miyazawa 3N forces (48) due to Δ excitations in the top panel (b) and (c) of Figure 3. This results from the interactions of two valence neutrons with any of the nucleons in the core, which corresponds to the normal-ordered two-body part of 3N forces, and the repulsive nature for valence neutrons is rather general (42). The dominance of the normal-ordered two-body part, which is enhanced by all core nucleons, can be understood based on phase-space arguments for normal Fermi systems (49) and was verified in explicit calculations (50, 51). The top panel (c) of Figure 3 shows that N^{2}LO 3N forces, fit to few-nucleon systems only, predict the dripline correctly. It is interesting to note that the same 3N forces also lead to repulsion in neutron matter, see Section 4.1.

This repulsive 3N-force mechanism was confirmed in more recent calculations based on large many-body spaces and with improved MBPT and nonperturbative valence-space Hamiltonians, as shown in the bottom panels of Figure 3. All results obtained in large many-body spaces with a SRG-evolved NN+3N-full Hamiltonian (27, 29, 40) (see the bottom right panel) lead to the correct dripline position at ^{24}O and the different many-body methods agree within a few percent. With NN+3N-ind forces only (not shown), all oxygen isotopes are underbound with respect to experiment and bound up to ^{28}O. The results obtained from ab initio valence-space Hamiltonians are shown in the bottom left panel of Figure 3. The nonperturbative calculations are in the sd shell, while the MBPT calculations are performed in an extended $sdf_{7/2}p_{3/2}$ valence space. In this case, the range of predictions is broader, but the 3N contributions also lead to an increased repulsion with neutron number. The broader range here is due to the different Hamiltonians considered (MBPT vs. IM-SRG/CCEI) as well as due to different many-body approximations.

2.2. Spectroscopy

Next, we discuss excited states in the neutron-rich oxygen isotopes ^{22,23,24}O, which have been the subject of recent experiments (52, 53, 54, 55, 56, 57). **Figure 4** compares the measured low-lying states with theoretical calculations for each nucleus. We note that the spectra of neutron-rich oxygen isotopes have also been calculated in CC theory with phenomenological 3N forces adjusted to the oxygen isotopes (3N$_{eff}$) and including the continuum (58), with good agreement to experiment. In Figure 4, we show only the CCEI results, as they are based on the same SRG-evolved interactions as in the IM-SRG calculations.

The first oxygen isotope with closed-shell properties for a non-standard magic number, ^{22}O, has its first 2^+ state at almost twice the energy as those in ^{18}O and ^{20}O. In contrast to ^{24}O, whose closed-shell nature can be qualitatively well described with NN forces due to the large separation between the $d_{3/2}$ and $s_{1/2}$ orbitals, the spectrum of ^{22}O is not well reproduced with NN forces: the first 2^+ state is below experiment, and the rest of the
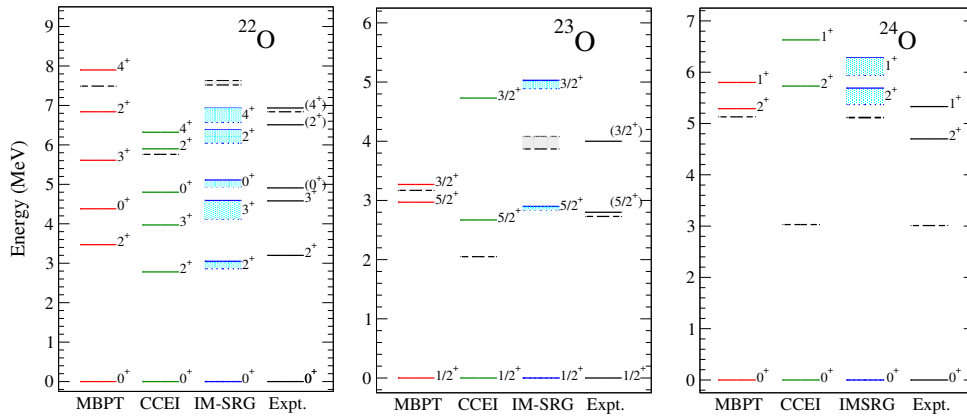
Figure 4

Excited-state spectra of ^{22,23,24}O based on NN+3N forces and compared with experiment. Figures adapted from (39). The MBPT results are performed in an extended $sdf_{7/2}p_{3/2}$ space (37) based on low-momentum NN+3N interactions, while the IM-SRG (39) and CCEI (40) results are in the sd shell from the SRG-evolved NN+3N-full Hamiltonian with $\hbar\omega = 20\,\mathrm{MeV}$ (CCEI and dotted IM-SRG) and $\hbar\omega = 24\,\mathrm{MeV}$ (solid IM-SRG). The dashed lines show the neutron separation energy.

spectrum is generally too compressed. Only when 3N forces are included, the 2^+ energy is in good agreement with experiment. Results with NN+3N forces are shown in Figure 4 for MBPT calculations in an extended $sdf_{7/2}p_{3/2}$ space (37) or with IM-SRG (39) and CCEI (40) in the sd shell. For the next excited states, the $2^+ - 3^+$ splitting is somewhat large in MBPT and results in an inversion of the 3^+ and 0^+ states and a too-even spacing of the other levels. This is not the case for IM-SRG and CCEI, where the level ordering is well reproduced and the spacings between states are close to experiment. Remarkably, the IM-SRG and CCEI results are within less than 200 keV when the same harmonic-oscillator value $\hbar\omega$ is used.

Of particular interest is the spectrum of ^{23}O, which provides a unique test for theory, as it simultaneously reflects the features of the doubly magic ^{22}O and ^{24}O. The shell model ^{23}O ground state is dominated by one particle in the $s_{1/2}$ orbit, while the two lowest excited states are expected to be a single-particle $5/2^+$ one-hole excitation, indicative of the strength of the ^{22}O shell closure, and a higher-lying single-particle $3/2^+$ one-particle excitation, reflecting the strength of the ^{24}O shell closure. The $5/2^+$ state lies just above the neutron decay threshold, while the $3/2^+$ state resides in the continuum. Reflecting the failure to reproduce the ^{22}O shell closure, all calculations with NN forces only predict a too low $5/2^+$ state. With 3N forces included, shown in the middle panel of Figure 4, the $5/2^+$ state is well reproduced in all calculations (37, 39, 40). The position of the $3/2^+$ state is approximately 1.0 MeV too low in MBPT and 1.0 MeV too high with IM-SRG and CCEI, which are again in remarkable agreement. The inclusion of the continuum is expected to lower the $d_{3/2}$ orbital (59) improving the IM-SRG and CCEI results.

Finally, the right panel of Figure 4 shows the spectrum of ^{24}O with 3N forces in comparison with experiment. All calculations find a clear closed-shell signature of a high 2^+ energy. Moreover, the spacing to the next 1^+ state is well reproduced. Note that due to the unbound $d_{3/2}$ orbital, continuum effects should be included (58).
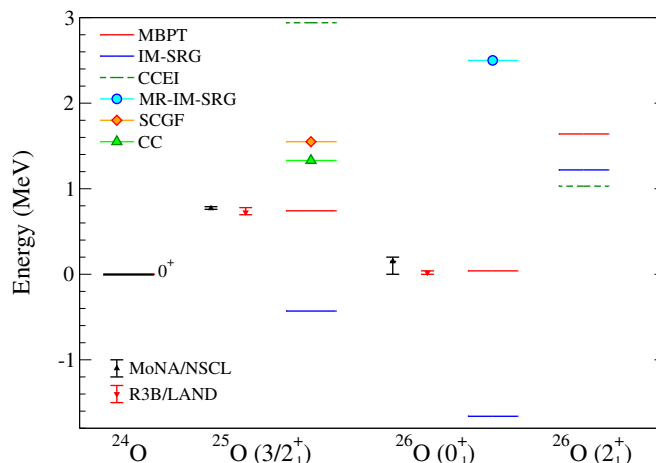
Figure 5

Ground-state energies of ^{25}O and ^{26}O relative to the ^{24}O ground state, and the energy of the first excited state in ^{26}O relative to the ^{26}O ground state. The experimental energies are from MoNA/NSCL (60, 61) and from R3B/LAND (62). Results are shown for the different many-body methods with NN+3N forces as in the bottom panels of Figure 3: MBPT including also residual 3N forces (62), IM-SRG (39), CCEI (40), MR-IM-SRG (27), SCGF (29), and CC (40).

2.3. Beyond the neutron dripline

Nuclei beyond the neutron dripline play an important role in understanding the behavior of extreme neutron-rich systems. The unbound ^{25}O and ^{26}O isotopes are the current experimental limits in oxygen (60, 61, 62), and the lifetime of ^{26}O makes it the first candidate to exhibit two-neutron radioactivity (63). A crucial aspect neglected in most of the calculations discussed here is the coupling to the continuum, which has been shown to play an important role for the physics of unbound states (64) and specifically for the oxygen isotopes (65). CC $3N_{eff}$ calculations found a typical contribution from continuum coupling to be on the order of 200 keV for the unbound states past ^{24}O.

Figure 5 compares the experimental ground-state energies of ^{25,26}O to theoretical predictions with NN+3N forces. In addition to the contribution from 3N forces to the SPEs and the two-body interactions of valence neutrons, the MBPT results shown (62) also include the small contribution from residual three-valence-neutron forces. These become more important with increasing neutron number along isotopic chains (49), with a repulsive contribution from $0.1 - 0.4$ MeV for $^{24-26}$O. For the ground state of ^{25}O, Figure 5 shows that MBPT, CC, and SCGF agree well with experiment, while the valence-space predictions from IM-SRG and CCEI are modestly too bound and unbound, respectively. For the ground state of ^{26}O only MBPT gives a result close to experiment. Nevertheless the overbinding seen in IM-SRG, and the underbinding obtained in MR-IM-SRG and CCEI (off the scale of the plot) are not unreasonable given expected theoretical uncertainties. Better agreement is found for the continuum shell model (65) and in CC $3N_{eff}$ calculations (58).

As shown in Figure 5, valence-space NN+3N calculations consistently predict a low first excited 2^+ state in ^{26}O between $1.0 - 1.6$ MeV. USDA and USDB interactions give a somewhat higher energy of 1.9 MeV and 2.1 MeV, respectively (44). Experimentally, events have been seen at 4 MeV (62), but in calculations the next state lies above 6 MeV due to
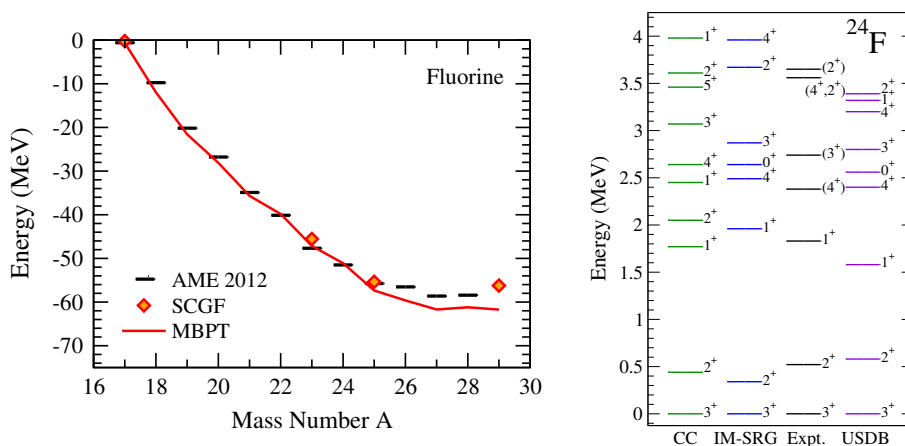
Figure 6

Left panel: Ground-state energies of fluorine isotopes measured from ^{16}O, compared to AME 2012 (45). The MBPT calculations (66) are performed in a proton sd and neutron $sdf_{7/2}p_{3/2}$ extended space based on low-momentum NN+3N forces, while the SCGF results (29) are with the SRG-evolved NN+3N-full Hamiltonian. Right panel: Excited-state spectrum of ^{24}F compared with experiment (67) and USDB (44). The CC results (41) are obtained in a large many-body space based on the optimized chiral NN+3N forces at N^{2}LO. The IM-SRG results (68) are calculated in the sd shell from the SRG-evolved NN+3N-full Hamiltonian.

the large $d_{3/2} - s_{1/2}$ gap. Note that the lowest excited states in ^{26}O have been very recently measured with high statistics at RIBF/RIKEN.

2.4. Neighboring open-shell nuclei

Fluorine isotopes have one more proton, and nuclear forces provide more binding mainly due to the tensor part. No predictions based on NN+3N forces exist for the dripline in fluorine, which lies at least as far as ^{31}F, but selected isotopes have been calculated from SCGF (29) and MBPT (66). These are shown in the left panel of **Figure 6**. Both SCGF and MBPT agree well with experiment through ^{25}F, with MBPT becoming modestly overbound beyond. Future experiments are needed to test the predictions beyond ^{28}F.

Large-scale CC results for excited states have been presented for ^{25,26}F (69, 70) with 3N$_{\text{eff}}$, and for ^{22,24}F with an optimized N^{2}LO NN+3N interaction (41). In addition, the spectrum of ^{24}F has been studied recently with the IM-SRG in comparison to new experimental results (67). These are shown in the right panel of Figure 6, where we also compare to USDB results. Without 3N forces (not shown), the spectrum is much too compressed and the ordering of levels is incorrect for both CC and IM-SRG: The first eight excited states lie below 2.0 MeV, in clear contrast to experiment. The NN+3N results for CC and IM-SRG shown in Figure 6 agree well with experiment, but differences are seen due to the different starting Hamiltonians. For CC the predicted first 2^+ and 1^+ states are well reproduced, but above these the density and ordering of states begins to deviate from tentative experimental spin-parity assignments. While the ground-state energy of ^{24}F is overbound by 7.7 MeV in IM-SRG, the predicted excited-state spectrum is in remarkably good agreement with the new experimental measurements, with all excited states below the one-neutron separation

threshold less than 200 keV away from experiment. The only exception is the 0^+ state at 2.6 MeV, also predicted by USDB, to which the experiment is not sensitive.

3. NEUTRON-RICH CALCIUM ISOTOPES

The calcium isotopes ($Z = 20$) provide an excellent region to study shell evolution from stability towards the neutron dripline. In addition to the standard doubly magic ^{40}Ca and ^{48}Ca, recent pioneering experiments at rare isotope beam facilities have explored new shell closures in exotic ^{52}Ca and ^{54}Ca (71, 72). The wealth of spectroscopic data on excited states and electromagnetic moments and transitions offers excellent tests for nuclear forces.

The calcium and neighboring isotopic chains lie at the frontier of theoretical calculations with 3N forces. Previous studies with phenomenological valence-space interactions (35, 73, 74) or beyond-mean-field calculations (75) provide a good description up to ^{52}Ca, but begin to disagree for more exotic isotopes where data was not available. This provides an additional motivation for calculations based on chiral EFT interactions.

The calcium isotopes $^{41-70}$Ca have been studied with MBPT in an extended $pfg_{9/2}$ valence space based on the same low-momentum NN+3N forces as for oxygen (76, 77, 71, 78, 79). The extended valence space compared to phenomenological interactions in the pf shell (35, 73, 74) suggests the need to treat the $g_{9/2}$ orbital nonperturbatively in MBPT calculations based on nuclear forces. Residual 3N forces between valence particles, which are important for very neutron-rich nuclei as discussed in Section 2.3, provide very small contributions for the calcium isotopes discussed here (71, 79). In addition to valence-space calculations, the calcium isotopes have been studied in large many-body spaces, where all nucleons are treated as active. The neutron-rich calcium isotopes from $^{47-62}$Ca (except for ^{57,58}Ca) have been calculated in CC theory with phenomenological 3N$_{\text{eff}}$ adjusted to the calcium isotopes (80, 81). In addition, SCGF (82) and MR-IM-SRG (83) provide results for even calcium isotopes isotopes based on the same SRG-evolved NN+3N-full Hamiltonian as for the oxygen isotopes. Finally, based on the same Hamiltonian, there are IT-NCSM results for the doubly magic ^{40,48}Ca (51).

The MBPT and CC results for the ground-state energies are in very good agreement with experiment (77, 71, 79, 80), while the SCGF (82) and MR-IM-SRG (83) both give overbound calcium isotopes, suggesting that the SRG-evolved NN+3N-full Hamiltonian is too attractive for heavier nuclei. Nevertheless this overbinding is systematic for all isotopes, and the experimental trend is reasonably reproduced.

3.1. Shell structure

The shell evolution along an isotopic chain can be studied with the two-neutron separation energy S_{2n}, where a significant decrease occurs past a shell closure. **Figure 7** compares the experimental S_{2n} with calculated MBPT (77, 71), CC (80), SCGF (82) and MR-IM-SRG (83) results. A first key feature in Figure 7 is the large decrease in S_{2n} from $N = 28$ to $N = 30$, a signature of the $N = 28$ magic number. This shell closure is not reproduced with NN forces only (76, 80, 35). First calculations with 3N forces (76, 80) showed that 3N forces are essential for the $N = 28$ shell closure. This also holds for the improved MBPT calculations of References (77, 71), shown in Figure 7, where 3N forces are included to third order in MBPT [3N forces were only included to first order in (76)]. While the ^{48}Ca S_{2n} has not been calculated in CC, the decrease from ^{49}Ca to ^{50}Ca reproduces experiment very
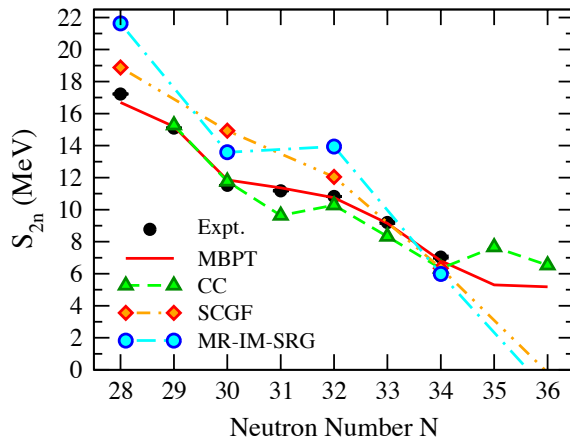
Figure 7

Two-neutron separation energy S_{2n} in neutron-rich calcium isotopes as a function of neutron number N. The experimental energies (45, 77, 71) are compared with MBPT predictions (77, 71) based on low-momentum NN+3N forces and CC theory with phenomenological $3N_{eff}$ (80). In addition, SCGF (82) and MR-IM-SRG (83) results are shown based on a SRG-evolved NN+3N-full Hamiltonian.

well. Also shown in Figure 7 are SCGF (82) and MR-IM-SRG (83) results, based on the same SRG-evolved NN+3N-full Hamiltonian, which somewhat underestimate (SCGF) or overestimate (MR-IM-SRG) the decrease in S_{2n} past $N = 28$.

The flat behavior in S_{2n} from $N = 30$ to $N = 32$ was predicted in calculations with 3N forces (76, 77), as well as with phenomenological shell-model interactions (73, 74). This was recently confirmed with precision Penning-trap mass measurements of ^{51,52}Ca at TITAN/TRIUMF (77), which found ^{52}Ca to be 1.74 MeV more bound. This represented the largest change in the atomic mass evaluation in the last ten years. More recently, the masses of ^{53,54}Ca were measured in pioneering multi-reflection time-of-flight mass measurement at ISOLTRAP/CERN (71). The resulting S_{2n} values show a decrease from $N = 32$ to $N = 34$, similar to the one past ^{48}Ca. This unambiguously establishes the doubly magic character of ^{52}Ca. The shell closure in calcium at $N = 32$ had already been suggested based on the first excited 2^+ energy in ^{52}Ca (84, 85) and nuclear spectroscopy (86, 87). Figure 7 shows that the experimental S_{2n} from $N = 32$ to $N = 34$ are in excellent agreement with the MBPT and CC predictions. We also observe that the different calculations with 3N forces start to deviate most in ^{56}Ca. Therefore, a future mass measurement of ^{56}Ca would provide a key test for theory, as well as direct information about the closed-shell nature of ^{54}Ca. Phenomenological shell-model interactions (73, 74) also provide a good description of S_{2n} to ^{54}Ca, while energy-density functionals (88) tend to predict an almost linear trend in S_{2n}, missing the steeper decrease at $N = 28$ and $N = 32$ (71).

Another key observable to assess shell evolution is the excitation energy of the first 2^+ state in the even isotopes. **Figure 8** shows the experimental energies compared to the available theoretical calculations with NN+3N forces: MBPT (78) and CC (80). The agreement of both calculations to experiment is very good, especially in capturing the high 2^+ energy in ^{48}Ca and ^{52}Ca, associated with the $N = 28$ and $N = 32$ shell closures. Especially interesting is the 2^+ energy in the exotic ^{54}Ca, recently measured at RIBF/RIKEN (72),

which is also in very good agreement with both MBPT and CC predictions. The relatively high energy of this 2^+ state, and the increase compared to other $N = 34$ isotones, suggests a shell closure in calcium at $N = 34$ (72).

From Figures 7 and 8, we see that the predictions of shell evolution are consistent when considering different observables. In addition, three-point mass differences, defined as $\Delta_n^{(3)} = \frac{(-1)^N}{2}[B(N+1, Z) + B(N-1, Z) - 2B(N, Z)]$ with (negative) ground-state energy $B(N, Z)$, provide another signature for shell evolution, with relative peaks in $\Delta_n^{(3)}$ associated with closed shells. When comparing MBPT results (78) for $\Delta_n^{(3)}$ with experiment, the trend with neutron number along the calcium chain is well reproduced, with peaks at $N = 28$ and $N = 32$, and an anomalously low $\Delta_n^{(3)}$ value for ^{53}Ca, placed between two shell closures and dominated by the low-j $p_{1/2}$ orbital (90).

With present calculations based on NN+3N forces, it is difficult to predict the neutron dripline because of the very flat behavior of the ground-state energies past ^{60}Ca found in energy-density functional calculations, MBPT, CC, and MR-IM-SRG (80, 79, 83, 91), so that very small interaction contributions can be decisive. In addition, for such weakly bound systems, the continuum, currently included only in CC, plays an important role (80), and should also be included in all calculations. Moreover, valence-space Hamiltonian for more exotic isotopes will have to consider the $1d_{5/2}$ and $2s_{1/2}$ orbitals (80, 92). Improved calculations towards the dripline will allow the exploration of a possible $N = 40$ shell closure in ^{60}Ca, which is the target of ongoing experimental efforts in neighboring isotopes (93). Finally, CC calculations combined with halo EFT have suggested interesting Efimov physics around ^{60}Ca, with the possibility of ^{62}Ca being a two-neutron halo nucleus (81).

In addition to the calcium results, SCGF calculations have been performed for the ground-state energies of Ar ($Z = 18$), K ($Z = 19$), Sc ($Z = 21$), and Ti ($Z = 22$) (82), and the resulting S_{2n} generally agree well with experiment, apart from an overestimated shell gap at $N = 20$ attributed to the NN+3N-full Hamiltonian used. In $^{37-49}$K, the evolution of the splitting between the lowest $1/2^+$ and $3/2^+$ states calculated with SCGF

also successfully describes experiment (94).

Finally, 3N forces provide similar repulsive contributions to the ground-state energies of the proton-rich $N = 20$ isotones, which have been studied in MBPT including the isospin-symmetry-breaking parts of chiral EFT interactions (95). Ground-state properties of heavier neutron-rich systems have also been explored in large-scale calculations with NN+3N forces. First MR-IM-SRG results along the nickel chain ($Z = 28$) (83), based on the same NN+3N-full Hamiltonian used in calcium, show a similar overbinding, also seen in CC calculations for doubly magic nuclei up to ^{132}Sn (96).

3.2. Spectroscopy

The study of shell evolution is complemented by exploring spectroscopic properties of calcium isotopes based on NN+3N forces. Spectra beyond 2^+ states based on chiral NN+3N forces have been obtained with MBPT (79) and with CC $3N_{\text{eff}}$ for states dominated by ground-state particle-hole excitations in $^{52-56}$Ca (80). Electromagnetic moments and transitions have also been calculated with MBPT (76, 79, 97).

The overall agreement of MBPT and CC spectra with experiment is good, with low-lying states in odd-mass nuclei consistent with the shell evolution discussed in Section 3.1. Some deficiencies are present, e.g., with too low $5/2^-$ states in ^{49,51}Ca in MBPT, but generally the results are similar to phenomenological interactions (79). Low-lying excited states in ^{42}Ti, calculated with MBPT (95), and in neutron-rich ^{52,54,56}Ti, obtained from CC (80), are also in good agreement with experiment. Future experiments with rare isotopes can test MBPT and CC predictions for several excited states in neutron-rich $^{52-56}$Ca. In addition, there are MBPT predictions for the mostly unexplored excited states in proton-rich $N = 20$ isotones up to ^{48}Ni (95).

Electromagnetic moments provide a complementary test of nuclear forces. **Figure 9** compares the experimental magnetic moments and electric quadrupole moments of neutron-rich calcium isotopes with MBPT predictions, including the very recent measurements at COLLAPS/ISOLDE (97). For comparison, the results with KB3G and GXPF1A interactions are also shown. The lower panel of Figure 9 shows the electric quadrupole moments. The experimental linear trend from ^{41}Ca to ^{47}Ca and ^{49}Ca to ^{51}Ca, a signature of the filling of the $f_{7/2}$ and $p_{3/2}$ orbitals, suggests that the quadrupole moments are dominated by the single-particle character of the ground states. The MBPT predictions exhibit a very good description of the experimental quadrupole moments, in general similar to KB3G and GXPF1A interactions and better for ^{47}Ca. Note that the theoretical results use the same neutron effective charges $e_n = 0.5e$ (97). Electric quadrupole transitions involving excited states in $^{46-50}$Ca have also been calculated in MBPT with the same effective charges (79). Similar to phenomenology, the agreement with experiment is reasonable, taking into account that the measured $B(E2)$ values vary within a factor of 50.

The upper panel of Figure 9 compares the experimental magnetic moments with theoretical results obtained with bare g-factors. Calculations for the lighter isotopes ^{41,43,45}Ca, which assume a ^{40}Ca core, do not reproduce experiment, suggesting the importance of sd-shell degrees of freedom for magnetic moments. This is in agreement with the g-factors of the 2^+ states in ^{42,44,46}Ca (98, 99), as well as calcium isotope shifts (100). For ^{47}Ca MBPT reproduces experiment well, and the predictions for neutron-rich ^{49}Ca and ^{51}Ca are in very good agreement with very recent measurements (97). Magnetic moments with phenomenological interactions are similar to MBPT except for ^{51}Ca, where the NN+3N calculation
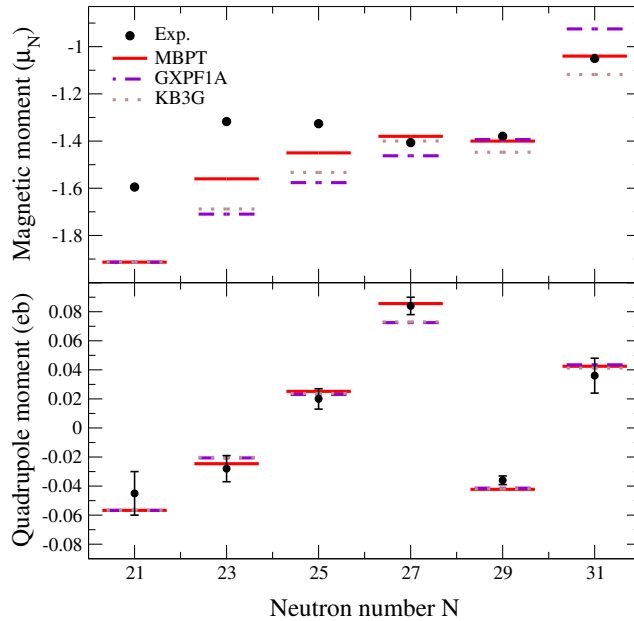
Figure 9

Magnetic moments (upper panel) and electric quadrupole moments (lower panel) of the odd calcium isotopes as a function of neutron number N. Experiment (97) is compared to MBPT calculations with low-momentum NN+3N forces in the $pfg_{9/2}$ valence space (97). For comparison, pf-shell calculations with phenomenological interactions KB3G (73) and GXPF1A (74) are shown. Figure adapted from (97).

lies between KB3G and GXPF1A.

The magnetic dipole $B(M1)$ strength in ^{48}Ca was first calculated with MBPT in Reference (76), with improvements in Reference (79) by including 3N forces to third order. The experimental peak at $10.2\,\text{MeV}$ (101) is very well reproduced in the MBPT calculation, but with too much strength, suggesting a modest quenching of $q = 0.9$ in the spin g-factor. Phenomenological interactions GXPF1A and KB3 also reproduce the concentrated peak and strength, but with a more substantial quenching of $q = 0.75$ (101).

This quenching is in contrast with the calculations of the magnetic moments in Figure 9, where the bare spin g-factors give a good description of experiment. This inconsistency and the sensitivities to different interactions in Figure 9 (compared to the smaller spread for the quadrupole moments) point to the need for systematic calculations of magnetic moment operators in the valence space. Necessary improvements are the inclusion of electromagnetic two-body currents (or meson-exchange currents), which are derived in chiral EFT consistently with nuclear forces, as well as controlled calculations of effective operators. Results with chiral two-body currents in light nuclei demonstrate that they provide significant contributions to magnetic moments (102), while first applications to medium-mass nuclei have focused on Gamow-Teller transitions (41, 103).

4. NEUTRON-RICH MATTER AND NEUTRON STARS

The physics of neutron-rich matter covers a wide range of extremes. At very low densities, the average interparticle distance is sufficiently large so that details of nuclear forces are not resolved and all properties of the system are governed by the large S-wave scattering length. In this universal regime, neutron matter shares many properties with cold atomic gases close to the unitary limit, which are the subject of active experimental and theoretical studies (104). At intermediate densities, which are most relevant for nuclei, the properties of neutron and nuclear matter are used to guide the development of energy density functionals, in particular to constrain the physics of neutron-rich systems, which are key for understanding the synthesis of heavy nuclei in the universe. At higher densities, far beyond nuclear densities, the composition and properties of nuclear matter are still unknown. Exotic states of matter containing strange particles or quark matter may be present. On the other hand, neutron matter constitutes also a unique laboratory for chiral EFT, because all many-body forces are predicted to N^3LO, see Section 1.2. This offers the possibility to derive reliable constraints based on chiral EFT interactions for the equation of state (EOS) of neutron-rich matter in astrophysics, for the symmetry energy and its density dependence, and for the structure of neutron stars, but also makes it possible to test the chiral EFT power counting and the hierarchy of many-body forces at densities relevant for nuclei.

The importance of chiral 3N forces for understanding and predicting nuclei has already been discussed in Sections 2 and 3. The same 3N forces play an important role for nuclear matter. In particular, the saturation of symmetric nuclear matter is driven by 3N forces (105, 15). While 3N contributions to neutron matter are smaller, they are crucial for the EOS of neutron-rich matter, and thus for the symmetry energy and its density dependence discussed in Section 4.2, and for neutron stars in Section 4.3.

4.1. Neutron matter properties and theoretical uncertainties

The left panel of **Figure 10** shows the energy per particle of neutron matter up to saturation density $n_0 = 0.16 \, \text{fm}^{-3}$. The results are obtained with different many-body methods based on chiral EFT interactions, all with the 500 MeV N^3LO potential (20) at the NN level. In case where the energy is shown with bands, for MBPT (red lines, cyan and blue band) (106, 108, 109) and SCGF (107) results, the theoretical uncertainty of the energy is dominated by uncertainties in the low-energy couplings c_1 and c_3, which determine the long-range two-pion-exchange parts of 3N forces, and not by truncations in the many-body calculation. The red lines and blue band show results including contributions from N^2LO 3N forces, whereas the cyan band includes all 3N and 4N interactions to N^3LO. In addition, for the blue band the NN potential has been RG-evolved to a low-momentum scale $\Lambda = 2.0 \, \text{fm}^{-1}$. We also show CC (110), MBPT of Reference (111), and SCGF (107) results, including N^2LO 3N forces. These all lie within the overlap of the blue and cyan band (except for the lowest density SCGF point, where the zero-temperature extrapolation may be difficult). The determination of the c_i couplings from πN scattering is consistent with the extraction from NN scattering, see, e.g., the discussion in (13), however with large uncertainties. Therefore, the c_i range for the bands in Figure 10 is taken conservatively: at N^2LO (red lines and blue band), $c_1 = (0.7 - 1.4) \, \text{GeV}^{-1}$ and $c_3 = (2.2 - 4.8) \, \text{GeV}^{-1}$ (116, 106) [with a similar c_i range for SCGF (107)], and at N^3LO (cyan band), $c_1 = -(0.75 - 1.13) \, \text{GeV}^{-1}$ and $c_3 = -(4.77 - 5.51) \, \text{GeV}^{-1}$ (117).

Figure 10 shows that chiral EFT interactions provide strong constraints on the EOS of
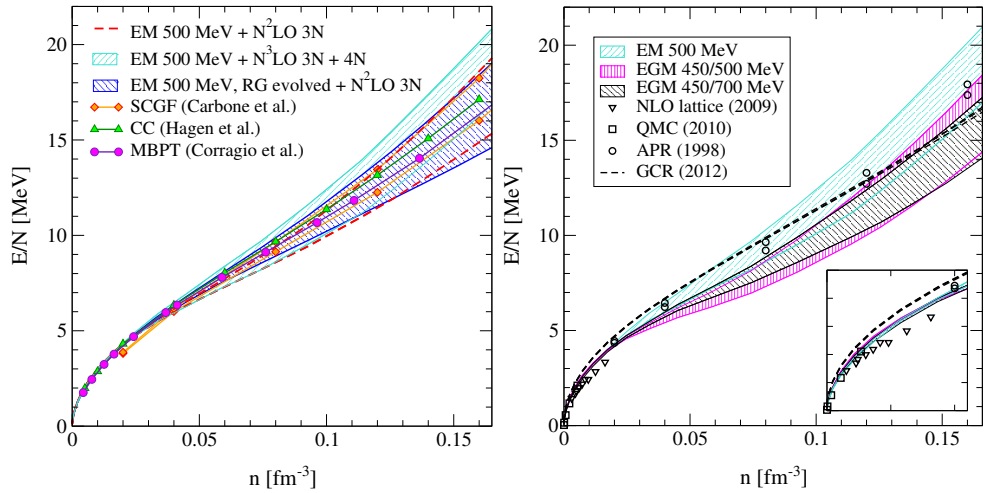
Figure 10

Energy per particle E/N of neutron matter as a function of density n based on different chiral EFT interactions and using different many-body methods The uncertainty bands in the left panel show the energy range based on the 500 MeV N^{3}LO NN potential of Reference (20) and including N^{2}LO 3N forces in MBPT (red lines) (106) or in the SCGF approach (107), as well as including all 3N and 4N interactions to N^{3}LO (108, 109) (cyan band). The blue band shows the results after RG-evolution of the NN potential (17, 106). In addition, we show results obtained in CC theory (110) and in MBPT of Corragio et al. (111). When bands are given, these are dominated by the uncertainties in the c_i couplings in 3N forces. Figure adapted from Reference (106). The right panel shows the energy per particle including NN, 3N and 4N forces at N^{3}LO based on different N^{3}LO potentials (cyan, magenta, and black bands). The bands include uncertainty estimates due to the many-body calculation, the c_i couplings, and by varying the 3N/4N cutoffs. For details see (108, 109). For comparison, results are shown at low densities (see also the inset) from NLO lattice (112) and quantum Monte Carlo (QMC) simulations (113), and at nuclear densities from variational (APR) (114) and auxiliary field diffusion Monte Carlo calculations (GCR) (115) based on 3N potentials adjusted to nuclear matter properties.

neutron matter, which are consistent among different many-body methods and considering variations of the Hamiltonian. The remarkable overlap of the red lines and the blue band indicates that neutron matter is, to a good approximation, perturbative for chiral NN interactions with $\Lambda \lesssim 500\,\text{MeV}$, see Reference (109) for details. This has been benchmarked by first quantum Monte Carlo calculations with local chiral EFT interactions (118, 119). In addition, there are calculations of neutron matter using in-medium chiral perturbation theory approaches with similar results (120, 121).

The right panel of Figure 10 shows the first complete N^{3}LO calculation of the neutron matter energy, which includes all NN, 3N and 4N interactions to N^{3}LO (108, 109). The energy range is based on different NN potentials, a variation of the c_i couplings (which dominates the total uncertainty), a 3N/4N-cutoff variation, and the uncertainty in the many-body calculation. We note that the individual 3N topologies at N^{3}LO (see Figure 2) give significant contributions to the energy (108, 109). The N^{3}LO range in the right panel of Figure 10 is in very good agreement with NLO lattice results (112) and quantum Monte Carlo calculations (113) at very low densities (see inset), where the properties are determined by the large scattering length and effective range (122). We also find a very good
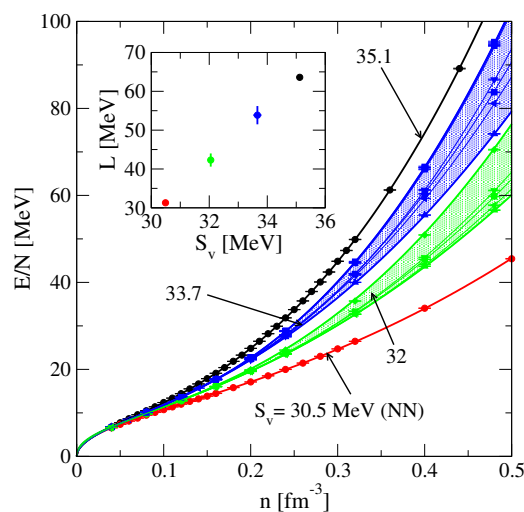
Figure 11

Energy per particle E/N of neutron matter as a function of density n obtained from quantum Monte Carlo calculations with phenomenological NN and 3N potentials (115), where the strength of the short-range 3N interactions is adjusted to the chosen values for the symmetry energy S_v. ($S_v = 30.5\,\text{MeV}$ is the symmetry energy obtained for this NN potential.) For each value of S_v, the band shows contributions of different 3N operator structures. The inset illustrates a correlation between S_v and the L parameter. For details see (115).

agreement with other ab initio calculations of neutron matter based on the Argonne NN and Urbana 3N potentials: The results based on variational calculations (APR) (114) are within the N^{3}LO band. In addition, the results from auxiliary field diffusion Monte Carlo calculations (GCR) (115) are shown based on nuclear force models adjusted to an energy difference of 32 MeV between neutron matter and the empirical saturation point, see **Figure 11**.

The properties of neutron matter impact the neutron distributions in nuclei. In particular, a higher neutron matter pressure at typical nuclear densities pushes neutrons further out and thus implies larger neutron skins (123, 124). Using these correlations the neutron matter results shown in Figure 10 (blue bands in the left panel) predict the neutron skin of ^{208}Pb to $0.17 \pm 0.03\,\text{fm}$ (116). This is in excellent agreement with the extraction of $0.156^{+0.025}_{-0.021}\,\text{fm}$ from the dipole polarizability (125). The theoretical uncertainty is also smaller than the target goal of a new PREX measurement using parity violating electron scattering at JLAB (126). Moreover, including properties of doubly magic nuclei as constraints, in addition to low-density neutron matter results, leads to even tighter predictions for the neutron skins of ^{208}Pb and ^{48}Ca to be $0.182 \pm 0.010\,\text{fm}$ and $0.173 \pm 0.005\,\text{fm}$, respectively (127).

4.2. Symmetry energy

The symmetry energy characterizes the behavior of the energy of nuclear matter as a function of proton fraction $x = n_p/n$ or asymmetry parameter $\beta = (N - Z)/A = (1 - 2x)$.

Table 1 Predicted range for the symmetry energy S_v and the L parameter, which determines the density dependence of the symmetry energy. The results (106) are obtained from neutron matter calculations based on chiral NN+3N forces using the expansion Equation 4 with different γ values, which lead to different incompressibilities K. As shown, the predicted ranges for S_v and L depend very weakly on γ. Also given is the predicted range for the L parameter based on quantum Monte Carlo calculations with phenomenological NN+3N potentials, where the strength of the short-range 3N interactions was adjusted to the chosen range for S_v (115) (see also Figure 11).

γ	K [MeV]	S_v [MeV]	L [MeV]
1.2	210	$29.7 - 32.8$	$32.4 - 53.4$
4/3	236	$29.7 - 33.2$	$32.5 - 57.0$
1.45	260	$30.1 - 33.5$	$33.6 - 56.7$
Gandolfi et al. (2011)		$32.0 - 35.1$	$40.6 - 63.6$

Around symmetric matter, the energy per particle can be expanded in the following form:

$$\frac{E(x,n)}{A} = \frac{E(0,n)}{A} + \beta^2 E_{\text{sym}}(n) + \dots . \tag{1}$$

Since the symmetry energy is a key quantity for the equation of state and for astrophysical applications, it has been subject of many experimental and theoretical studies (128, 129, 130). Sometimes the above expansion is truncated after the quadratic term, however, in general the symmetry energy S_v is defined as the second derivate with respect to proton fraction,

$$S_v = \frac{1}{8} \left. \frac{\partial^2 E/A(\bar{n},x)}{\partial x^2} \right|_{\bar{n}=1,x=1/2}, \tag{2}$$

where $\bar{n} = n/n_0$ is the density in units of the saturation density. Another important quantity for astrophysics is the density dependence of the symmetry energy, characterized by the L parameter,

$$L = \frac{3}{8} \left. \frac{\partial^3 E/A(\bar{n},x)}{\partial \bar{n} \partial x^2} \right|_{\bar{n}=1,x=1/2}. \tag{3}$$

To obtain S_v and L it is necessary to extend the microscopic calculations to finite proton fractions. This can be achieved by either performing calculations for several different asymmetries or by using neutron matter and symmetric nuclear matter as anchor points and interpolating these results to arbitrary proton fractions. One such interpolation has been used in Reference (106), with an empirical parameterization that includes kinetic energy terms plus an interaction energy that is quadratic in the neutron excess $1 - 2x$:

$$\frac{E/A(\bar{n},x)}{T_0} = \frac{3}{5} \left[x^{5/3} + (1-x)^{5/3} \right] (2\bar{n})^{2/3}$$

$$- \left[(2\alpha - 4\alpha_L)x(1-x) + \alpha_L \right] \bar{n} + \left[(2\eta - 4\eta_L)x(1-x) + \eta_L \right] \bar{n}^\gamma . \tag{4}$$

Here, $T_0 = 36.84\,\text{MeV}$ is the Fermi energy of symmetric nuclear matter at the saturation density. The parameters α, η, α_L, and η_L can be determined from the empirical saturation properties of symmetric nuclear matter combined with microscopic calculations of neutron matter (106). This strategy takes advantage of the fact that the theoretical uncertainties
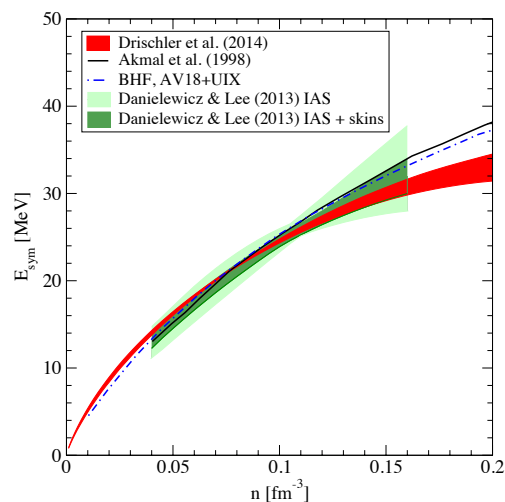
Figure 12

Symmetry energy as a function of density n obtained from ab initio calculations of asymmetric matter based on chiral NN+3N forces (135) (red band), from microscopic calculations performed with a variational approach [Akmal et al. (1998)] (114) and from Brueckner-Hartree-Fock calculations (BHF) (136) based on the Argonne v_{18} NN and Urbana UIX 3N potentials (with parameters adjusted to the empirical saturation point). For comparison, the band over the density range $n = 0.04 - 0.16\,\mathrm{fm}^{-3}$ is based on an analysis of isobaric analog states (IAS) and including the constraints from neutron skins (IAS + skins) (137). Figure taken from (135).

of neutron matter calculations are significantly smaller than for systems with finite proton fractions. As shown in **Table 1**, the predicted range for S_v and L depends only weakly on the particular choice of γ, which is correlated with the incompressibility. Also given is the predicted range for the L parameter obtained from quantum Monte Carlo calculations (115) based on 3N potentials adjusted to the chosen range of S_v. Figure 11 shows these results for neutron matter in more detail, highlighting the correlation between S_v and L. It is remarkable how well the $S_v - L$ regions in Table 1 agree, given the very different Hamiltonians used in the quantum Monte Carlo calculations.

The $S_v - L$ predictions based on NN+3N forces agree well with constraints obtained from energy density functionals for nuclear masses (131) and from the ^{208}Pb dipole polarizability (125). In addition, there is good agreement with studies of the Sn neutron skin (132), of giant dipole resonances (133), and with an estimate obtained from modeling X-ray bursts and quiescent low-mass X-ray binaries (134). A detailed discussion can be found in Reference (129).

Recently, the symmetry energy has also been studied in ab initio calculations of asymmetric matter at small proton fractions based on chiral EFT interactions (135). The energy of asymmetric matter was found to compare very well with the quadratic expansion even for neutron-rich conditions, which was then used to extract the quadratic symmetry energy term E_{sym}. In addition, the results were used to benchmark the empirical parameterization, Equation 4, with very good agreement. In contrast to other calculations, the results are based on 3N forces fit only to light nuclei, without adjustments to empirical nuclear matter properties. The results for E_{sym} are compared in **Figure 12** with constraints from

a recent analysis of isobaric analog states (IAS) and including the constraints from neutron skins (IAS + skins) (137), showing a remarkable agreement over the entire density range. Compared to extracting the symmetry energy from neutron matter calculations using the empirical parameterization, Equation 4, the uncertainty is reduced due to the explicit information from asymmetric matter.

4.3. Neutron stars

The structure of nonrotating neutron stars can be studied by solving the Tolman-Oppenheimer-Volkov equations (138), based on an EOS of neutron star matter, i.e., matter in beta-equilibrium. The proton fraction x for matter under these conditions is determined by minimizing, for a given nucleon density, the total energy per particle plus the contributions from electrons and from the rest mass of the nucleons. The resulting proton fractions are of the order $x \approx 5\%$ (116, 106).

Since the central densities of neutron stars can significantly exceed the regime for which reliable microscopic nuclear matter calculations are possible, it is necessary to extend the EOS systematically to higher densities. This can be achieved by using microscopic results up to a maximal density and employing general piecewise polytropic extensions beyond (116, 106). This strategy allows for soft regions and generates a complete set of possible EOSs at high densities, independent of the assumptions on the interactions and constituents of matter at high densities. In the end only those EOS are retained that (a) remain causal for all relevant densities, and (b) are able to support a neutron star mass $M = \widehat{M}$, the mass of the heaviest observed neutron star.

The left panel of **Figure 13** shows the resulting uncertainty band for the pressure as a function of mass density. The blue band at lower densities represents the pressure predicted for matter in beta equilibrium based on chiral EFT interactions (see red dashed lines in the left panel of Figure 10). The bands at higher densities give the EOS range, which is the envelope of all allowed polytropes at higher densities. The lighter blue band at high densities corresponds to the mass constraint $\widehat{M} = 1.97 M_\odot$, the central value of the two-solar-mass neutron star measured by Shapiro delay (139) and the lower 1σ mass of the recently observed most massive neutron star from radio timing observations (140), whereas the darker blue band corresponds to $\widehat{M} = 2.4 M_\odot$, a fictitious heavier neutron star. Obviously, the higher the mass of the heaviest neutron star observed, the stronger the EOS band is constrained. This uncertainty band is compared with a representative set of EOSs used in the literature. This set contains EOSs calculated within diverse theoretical approaches and based on different degrees of freedom. For details and notation we refer to Reference (141). We find that a significant number of EOSs are not compatible with the lower density band based on chiral EFT interactions. In addition, at higher densities only very few EOSs, including the variational EOSs based on phenomenological nuclear potentials (114) AP3 and AP4 in the left panel of Figure 13, are within the uncertainty bands over the entire density range. Finally, these constraints imply that a $1.4\,(1.97)\,M_\odot$ neutron star does not exceed densities beyond $4.4\,(7.6)\,n_0$, which corresponds to a Fermi momentum of only $550\,(660)\,\mathrm{MeV}$.

The EOS bands directly translate into constraints for the radii of neutron stars. In the right panel of Figure 13 we present the radius constraints obtained from the EOS bands shown in the left panel for the case $\widehat{M} = 1.97\,M_\odot$ (blue dashed lines) and the corresponding bands based on complete N^{3}LO calculations shown in the right panel of Figure 10 (red
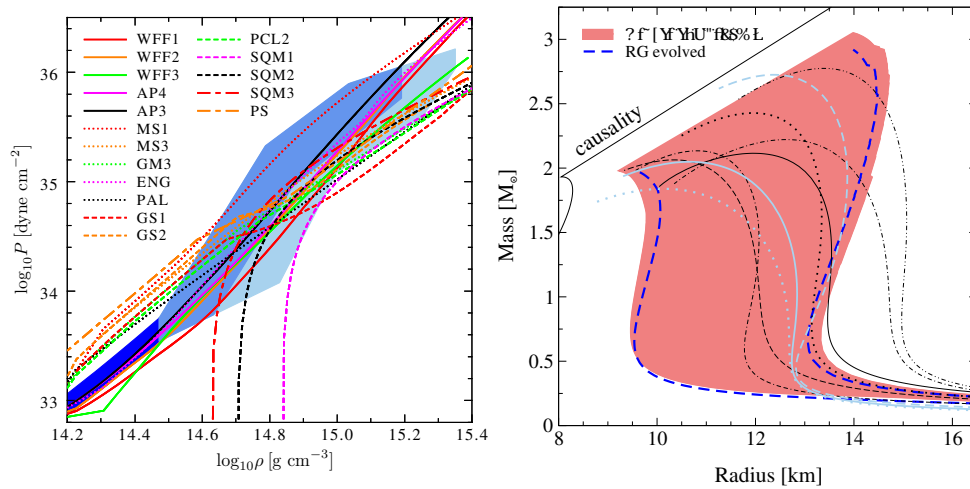
Figure 13

Left panel: Constraints for the pressure P of neutron star matter as a function of mass density ρ compared to EOSs commonly used to model neutron stars (141). The blue band at low densities represents the pressure predicted by the neutron matter results of Figure 10 (red lines of the left panel) and incorporating beta equilibrium. The bands at high densities are the envelope of general polytropic extensions that are causal and support a neutron star of mass $\widehat{M} = 1.97\,M_\odot$ (light blue band) and $\widehat{M} = 2.4\,M_\odot$ (darker blue band). For details see (106). Right panel: Constraints on the mass-radius diagram of neutron stars based on the N^{3}LO neutron matter results of Figure 10 (right panel) and following (106) for the extension to neutron-star matter and to high densities (red band), in comparison to the constraints based on RG-evolved NN interactions and 3N forces at N^{2}LO (thick dashed blue lines, based on the 1.97 $M_\odot$ band of the left panel). We also show the mass-radius relations obtained from EOSs for supernova simulations. For details see (109).

band). The radius uncertainty band represents an envelope of a large number of individual EOS reflecting the uncertainties at low densities and in the polytropic extensions to high densities (106, 109).The results of Figure 13 predict a radius range of $9.7 - 13.9\,\mathrm{km}$ for a $1.4\,M_\odot$ neutron star based on the complete N^{3}LO calculations. The largest supported neutron-star mass is found to be $3.1\,M_\odot$, with a corresponding radius of about $14\,\mathrm{km}$. These results agree very well with the mass-radius constraints from the neutron matter calculations based on RG-evolved NN interactions with N^{2}LO 3N forces. Furthermore, the radius constraints are also consistent with astrophysical extractions obtained from modeling X-ray burst sources, see, e.g., Reference (134).

For astrophysical applications it is crucial to reduce the theoretical uncertainties of the EOS over the entire density range shown in the left panel of Figure 13. At lower densities this requires improved estimates and a reduction of the theoretical uncertainties in nuclear forces. Specifically, this involves the inclusion of higher-order contributions in the chiral expansion, systematic order-by-order convergence studies, as well as improved determinations of the low-energy couplings. At higher densities, novel observations are expected to provide new and model-independent constraints: On the one hand, the observation of heavier neutron stars leads to a systematic reduction of the uncertainties, as illustrated in the left panel of Figure 13. On the other hand, astrophysical information on neutron star radii will provide significant constraints on the EOS. In particular, the gravitational wave signal from mergers

of binary neutron stars (142, 143, 144, 145) and neutron star-black hole mergers (146) has been shown to be sensitive to properties of the EOS at high densities and to neutron star radii. Hence, a detection with, e.g., advanced LIGO (147) will significantly improve our knowledge of the EOS in this regime. Moreover, future observations with the Neutron star Interior Composition ExploreR (NICER) and the Large Observatory for X-Ray Timing (LOFT) offer completely new perspectives for measuring neutron star radii. This will in turn provide important insights into nuclear forces at neutron-rich extremes.

5. SUMMARY AND OUTLOOK

We have shown that the physics of 3N forces connects neutron-rich nuclei with neutron-rich matter in neutron stars. The main features discussed in this review can be summarized by 3N forces having two effects for neutron-rich systems: first, 3N forces provide a repulsive central interaction, which drives saturation and leads to a stiffening of the neutron matter equation of state with increasing density. The same repulsion is important for the contributions from 3N forces to the ground-state energies that are key for the location of the neutron dripline. Second, 3N forces provide an attractive spin-orbit interaction, which increases the spin-orbit splittings and gives rise to the associated magic numbers, e.g., at $N = 28$. This physics and its interplay with the repulsive central interaction is at play for the formation and evolution of shell structure and for the spectroscopy of neutron-rich nuclei discussed in this review. The experimental discoveries for neutron-rich oxygen and calcium isotopes show that 3N forces provide an exciting link between the theoretical frontier in effective field theories and many-body methods with the exploration of exotic nuclei at rare isotope beam facilities worldwide. Three-nucleon forces are also key for the properties of neutron-rich matter at nuclear densities, which impacts the neutron skin, the symmetry energy, and the structure of neutron stars, in particular their radii.

Finally, we list a number of open problems and opportunities. First, it is important to study the order-by-order convergence in chiral EFT, and to carry out first complete N^{3}LO calculations of nuclei. This is especially important, because the Q^4 contributions are known to be important for an accurate reproduction of NN phase shifts at energies relevant to nuclei. It is crucial to study the theoretical uncertainties due to the truncation in chiral EFT, due to uncertainties in the low-energy couplings in NN and 3N forces, and due to the many-body calculation. While the latter has been well documented for many approaches and with benchmarks (see, e.g., the remarkable agreement for the same Hamiltonian with different ab initio methods discussed here), the theoretical uncertainties in the Hamiltonian have been less explored. Because most calculations so far are based on the N^{3}LO potential of Reference (20), it is also necessary to explore different NN potentials and many new developments in chiral EFT, including the optimized potentials of References (41, 148), new local chiral potentials (119), and improved chiral potentials of Reference (149), all with corresponding 3N forces. In addition, it is important to explore improved power counting schemes (e.g., see the discussion in Reference (150)) and to investigate nuclear forces with explicit Δ degrees of freedom (151, 152). Moreover, the discussed results show that additional work is needed to quantify the theoretical uncertainties, especially due to the truncation in chiral EFT (153), which is particularly relevant to the long-range parts of 3N forces due to the large c_i values.

Important advances for ab initio calculations are the investigation of open-shell nuclei with a range of many-body methods, the inclusion of the continuum for loosely bound

and resonant states close to the dripline (64, 58), the study of electroweak transitions with effective operators and consistent two-body currents based on chiral EFT (154, 103, 102, 41), extending the calculations to heavier nuclei with a controlled convergence in terms of 3N matrix elements included, and the reduction of uncertainties in the equation of state to further constrain the properties of neutron-rich matter and neutron-stars. Finally, it would be very interesting to transport the knowledge and constraints from nuclear forces to density functional calculations of all nuclei, especially regarding the structures of 3N forces and their impact on neutron-rich systems.

DISCLOSURE STATEMENT

The authors are not aware of any affiliations, memberships, funding, or financial holdings that might be perceived as affecting the objectivity of this review.

ACKNOWLEDGMENTS

LITERATURE CITED

1. Epelbaum E, Hammer HW, Meißner UG. *Rev. Mod. Phys.* 81:1773 (2009)
2. Machleidt R, Entem DR. *Phys. Rept.* 503:1 (2011)
3. van Kolck U. *Phys. Rev. C* 49:2932 (1994)
4. Epelbaum E, et al. *Phys. Rev. C* 66:064001 (2002)
5. Bernard V, Epelbaum E, Krebs H, Meißner UG. *Phys. Rev. C* 77:064004 (2008)
6. Bernard V, Epelbaum E, Krebs H, Meißner UG. *Phys. Rev. C* 84:054001 (2011)
7. Epelbaum E. *Phys. Lett. B* 639:456 (2006)
8. Beane SR, Detmold W, Orginos K, Savage MJ. *Prog. Part. Nucl. Phys.* 66:1 (2011)
9. Briceño RA, Davoudi Z, Luu TC. *J. Phys. G* 42:023101 (2015)
10. Ekström A, et al. *Phys. Rev. Lett.* 110:192502 (2013)
11. Bogner SK, Furnstahl RJ, Schwenk A. *Prog. Part. Nucl. Phys.* 65:94 (2010)
12. Furnstahl RJ, Hebeler K. *Rept. Prog. Phys.* 76:126301 (2013)
13. Hammer HW, Nogga A, Schwenk A. *Rev. Mod. Phys.* 85:197 (2013)
14. Gazit D, Quaglioni S, Navratil P. *Phys. Rev. Lett.* 103:102502 (2009)
15. Hebeler K, et al. *Phys. Rev. C* 83:031301(R) (2011)
16. Hebeler K, et al. *Phys. Rev. C* 91:044001 (2015)
17. Hebeler K, Schwenk A. *Phys. Rev. C* 82:014314 (2010)
18. Kalantar-Nayestanaki N, Epelbaum E, Messchendorp JG, Nogga A. *Rept. Prog. Phys.* 75:016301 (2012)
19. Golak J, et al. *Eur. Phys. J. A* 50:177 (2014)

20. Entem DR, Machleidt R. *Phys. Rev. C* 68:041001(R) (2003)
21. Jurgenson ED, Navrátil P, Furnstahl RJ. *Phys. Rev. Lett.* 103:082501 (2009)
22. Roth R, Calci A, Langhammer J, Binder S. *Phys. Rev. C* 90:024325 (2014)
23. Navrátil P. *Few Body Syst.* 41:117 (2007)
24. Hagen G, Papenbrock T, Hjorth-Jensen M, Dean DJ. *Rept. Prog. Phys.* 77:096302 (2014)
25. Tsukiyama K, Bogner SK, Schwenk A. *Phys. Rev. Lett.* 106:222502 (2011)
26. Hergert H, et al. *Phys. Rev. C* 87:034307 (2013)
27. Hergert H, et al. *Phys. Rev. Lett.* 110:242501 (2013)
28. Barbieri C, Hjorth-Jensen M. *Phys. Rev. C* 79:064313 (2009)
29. Cipollone A, Barbieri C, Navrátil P. *Phys. Rev. Lett.* 111:062501 (2013)
30. Somà V, Duguet T, Barbieri C. *Phys. Rev. C* 84:064317 (2011)
31. Somà V, Barbieri C, Duguet T. *Phys. Rev. C* 87:011303 (2013)
32. Roth R. *Phys. Rev. C* 79:064324 (2009)
33. Roth R, et al. *Phys. Rev. Lett.* 107:072501 (2011)
34. Epelbaum E, et al. *Phys. Rev. Lett.* 112:102501 (2014)
35. Caurier E, et al. *Rev. Mod. Phys.* 77:427 (2005)
36. Hjorth-Jensen M, Kuo TTS, Osnes E. *Phys. Rept.* 261:125 (1995)
37. Holt JD, Menéndez J, Schwenk A. *Eur. Phys. J. A* 49:39 (2013)
38. Tsukiyama K, Bogner SK, Schwenk A. *Phys. Rev. C* 85:061304(R) (2012)
39. Bogner SK, et al. *Phys. Rev. Lett.* 113:142501 (2014)
40. Jansen GR, et al. *Phys. Rev. Lett.* 113:142502 (2014)
41. Ekström A, et al. *Phys. Rev. Lett.* 113:262504 (2014)
42. Otsuka T, et al. *Phys. Rev. Lett.* 105:032501 (2010)
43. Utsuno Y, et al. *Phys. Rev. C* 70:044307 (2004)
44. Brown BA, Richter WA. *Phys. Rev. C* 74:034315 (2006)
45. Wang M, et al. *Chin. Phys. C* 36:1603 (2012)
46. Zuker AP. *Phys. Rev. Lett.* 90:042502 (2003)
47. Schwenk A, Holt JD. *AIP Conf. Proc.* 1011:159 (2008)
48. Fujita J, Miyazawa H. *Prog. Theor. Phys.* 17:360 (1957)
49. Friman B, Schwenk A. In *From Nuclei to Stars: Festschrift in Honor of Gerald E. Brown*, Ed. S. Lee (World Scientific, 2011) arXiv:1101.4858
50. Hagen G, et al. *Phys. Rev. C* 76:034302 (2007)
51. Roth R, et al. *Phys. Rev. Lett.* 109:052501 (2012)
52. Stanoiu M, et al. *Phys. Rev. C* 69:034312 (2004)
53. Fernandez-Dominguez B, et al. *Phys. Rev. C* 84:011301 (2011)
54. Elekes Z, et al. *Phys. Rev. Lett.* 98:102502 (2007)
55. Schiller A, et al. *Phys. Rev. Lett.* 99:112501 (2007)
56. Hoffman CR, et al. *Phys. Lett. B* 672:17 (2009)
57. Tshoo K, et al. *Phys. Rev. Lett.* 109:022501 (2012)
58. Hagen G, et al. *Phys. Rev. Lett.* 108:242501 (2012)
59. Tsukiyama K, Hjorth-Jensen M, Hagen G. *Phys. Rev. C* 80:051301 (2009)
60. Hoffman CR, et al. *Phys. Rev. Lett.* 100:152502 (2008)
61. Lunderberg E, et al. *Phys. Rev. Lett.* 108:142503 (2012)
62. Caesar C, et al. *Phys. Rev. C* 88:034313 (2013)
63. Kohley Z, et al. *Phys. Rev. Lett.* 110:152501 (2013)
64. Michel N, Nazarewicz W, Ploszajczak M, Vertse T. *J. Phys. G* 36:013101 (2009)
65. Volya A, Zelevinsky V. *Phys. Rev. Lett.* 94:052501 (2005)
66. Simonis J, Holt JD, Menéndez J, Schwenk A. In preparation (2015)
67. Cáceres L, et al. *Phys. Rev. C* 92:014327 (2015)
68. Bogner SK, Hergert H, Holt JD, Schwenk A. In preparation (2015)
69. Lepailleur A, et al. *Phys. Rev. Lett.* 110:082502 (2013)

70. Vajta Z, et al. *Phys. Rev. C* 89:054323 (2014)
71. Wienholtz F, et al. *Nature* 498:346 (2013)
72. Steppenbeck D, et al. *Nature* 502:207 (2013)
73. Poves A, Sanchez-Solano J, Caurier E, Nowacki F. *Nucl. Phys. A* 694:157 (2001)
74. Honma M, Otsuka T, Brown BA, Mizusaki T. *Eur. Phys. J. A* 25:499 (2005)
75. Rodriguez TR, Egido JL. *Phys. Rev. Lett.* 99:062501 (2007)
76. Holt JD, Otsuka T, Schwenk A, Suzuki T. *J. Phys. G* 39:085111 (2012)
77. Gallant AT, et al. *Phys. Rev. Lett.* 109:032506 (2012)
78. Holt JD, Menéndez J, Schwenk A. *J. Phys. G* 40:075105 (2013)
79. Holt JD, Menéndez J, Simonis J, Schwenk A. *Phys. Rev. C* 90:024312 (2014)
80. Hagen G, et al. *Phys. Rev. Lett.* 109:032502 (2012)
81. Hagen G, Hagen P, Hammer HW, Platter L. *Phys. Rev. Lett.* 111:132501 (2013)
82. Somà V, et al. *Phys. Rev. C* 89:061301(R) (2014)
83. Hergert H, et al. *Phys. Rev. C* 90:041302(R) (2014)
84. Huck A, Klotz G, Knipper A, et al. *Phys. Rev. C* 31:2226 (1985)
85. Gade A, et al. *Phys. Rev. C* 74:021302 (2006)
86. Mantica PF, et al. *Phys. Rev. C* 77:014313 (2008)
87. Crawford HL, et al. *Phys. Rev. C* 82:014311 (2010)
88. Erler J, et al. *Nature* 486:509 (2012)
89. http://www.nndc.bnl.gov/ensdf/
90. Brown BA. *Phys. Rev. Lett.* 111:162502 (2013)
91. Forssén C, et al. *Phys. Scr. T* 152:014022 (2013)
92. Lenzi SM, Nowacki F, Poves A, Sieja K. *Phys. Rev. C* 82:054301 (2010)
93. Gade A, et al. *Phys. Rev. Lett.* 112:112503 (2014)
94. Papuga J, et al. *Phys. Rev. C* 90:034321 (2014)
95. Holt JD, Menéndez J, Schwenk A. *Phys. Rev. Lett.* 110:022502 (2013)
96. Binder S, Langhammer J, Calci A, Roth R. *Phys. Lett. B* 736:119 (2014)
97. Garcia Ruiz RF, et al. *Phys. Rev. C* 91:041304(R) (2015)
98. Schielke S, et al. *Phys. Lett. B* 571:29 (2003)
99. Taylor MJ, et al. *Phys. Lett. B* 605:265 (2005)
100. Caurier E, et al. *Phys. Lett. B* 522:240 (2001)
101. von Neumann-Cosel P., Poves A, Retamosa J, Richer A. *Phys. Lett. B* 443:1 (1998)
102. Pastore S, Pieper SC, Schiavilla R, Wiringa R. *Phys. Rev. C* 87:035503 (2013)
103. Menendez J, Gazit D, Schwenk A. *Phys. Rev. Lett.* 107:062501 (2011)
104. Zwerger W. (Ed.) *The BCS-BEC Crossover and the Unitary Fermi Gas*, Lecture Notes in Physics, Volume 836. (Springer, Berlin, Heidelberg 2012)
105. Bogner SK, Schwenk A, Furnstahl RJ, Nogga A. *Nucl. Phys. A* 763:59 (2005)
106. Hebeler K, Lattimer JM, Pethick CJ, Schwenk A. *Astrophys. J.* 773:11 (2013)
107. Carbone A, Rios A, Polls A. *Phys. Rev. C* 90:054322 (2014)
108. Tews I, Krüger T, Hebeler K, Schwenk A. *Phys. Rev. Lett.* 110:032504 (2013)
109. Krüger T, Tews I, Hebeler K, Schwenk A. *Phys. Rev. C* 88:025802 (2013)
110. Hagen G, et al. *Phys. Rev. C* 89:014319 (2014)
111. Coraggio L, et al. *Phys. Rev. C* 87:014322 (2013)
112. Epelbaum E, Krebs H, Lee D, Meißner UG. *Eur. Phys. J. A* 40:199 (2009)
113. Gezerlis A, Carlson J. *Phys. Rev. C* 81:025803 (2010)
114. Akmal A, Pandharipande VR, Ravenhall DG. *Phys. Rev. C* 58:1804 (1998)
115. Gandolfi S, Carlson J, Reddy S. *Phys. Rev. C* 85:032801 (2012)
116. Hebeler K, Lattimer JM, Pethick CJ, Schwenk A. *Phys. Rev. Lett.* 105:161102 (2010)
117. Krebs H, Gasparyan A, Epelbaum E. *Phys. Rev. C* 85:054006 (2012)
118. Gezerlis A, et al. *Phys. Rev. Lett.* 111:032501 (2013)
119. Gezerlis A, et al. *Phys. Rev. C* 90:054323 (2014)

120. Holt JW, Kaiser N, Weise W. *Prog. Part. Nucl. Phys.* 73:35 (2013)
121. Lacour A, Oller JA, Meißner UG. *Ann. Phys.* 326:241 (2011)
122. Schwenk A, Pethick CJ. *Phys. Rev. Lett.* 95:160401 (2005)
123. Brown BA. *Phys. Rev. Lett.* 85:5296 (2000)
124. Typel S, Brown BA. *Phys. Rev. C* 64:027302 (2001)
125. Tamii A, et al. *Phys. Rev. Lett.* 107:062502 (2011)
126. Abrahamyan S, et al. *Phys.Rev.Lett.* 108:112502 (2012)
127. Brown BA, Schwenk A. *Phys. Rev. C* 89:011307 (2014)
128. Tsang MB, et al. *Phys. Rev. C* 86:015803 (2012)
129. Lattimer JM, Lim Y. *Astrophys. J.* 771:51 (2013)
130. Li BA, Ramos A, Verde G, Vidana I. *Eur. Phys. J. A* 50:9 (2014)
131. Kortelainen M, et al. *Phys. Rev. C* 82:024313 (2010)
132. Chen LW, Ko CM, Li BA, Xu J. *Phys. Rev. C* 82:024321 (2010)
133. Trippa L, Colo G, Vigezzi E. *Phys. Rev. C* 77:061304 (2008)
134. Steiner AW, Lattimer JM, Brown EF. *Astrophys. J.* 722:33 (2010)
135. Drischler C, Somà V, Schwenk A. *Phys. Rev. C* 89:025806 (2014)
136. Taranto G, Baldo M, Burgio GF. *Phys. Rev. C* 87:045803 (2013)
137. Danielewicz P, Lee J. *Nucl. Phys. A* 922:1 (2014)
138. Oppenheimer JR, Volkoff GM. *Phys. Rev.* 55:374 (1939)
139. Demorest P, et al. *Nature* 467:1081 (2010)
140. Antoniadis J, et al. *Science* 340:1233232 (2013)
141. Lattimer JM, Prakash M. *Astrophys. J.* 550:426 (2001)
142. Andersson N, et al. *Gen. Rel. Grav.* 43:409 (2011)
143. Bauswein A, Janka HT. *Phys. Rev. Lett.* 108:011101 (2012)
144. Bauswein A, Janka HT, Hebeler K, Schwenk A. *Phys. Rev. D* 86:063001 (2012)
145. Takami K, Rezzolla L, Baiotti L. *Phys. Rev. Lett.* 113:091104 (2014)
146. Lackey BD, et al. *Phys. Rev. D* 85:044061 (2012)
147. The LIGO Scientific Collaboration. *Class. Quant. Grav.* 32:074001 (2015)
148. Carlsson BD, et al. arXiv:1506.02466
149. Epelbaum E, Krebs H, Meißner UG. *Eur. Phys. J. A* 51:53 (2015)
150. Nogga A, Timmermans RGE, van Kolck U. *Phys. Rev. C* 72:054006 (2005)
151. Krebs H, Epelbaum E, Meißner UG. *Eur. Phys. J. A* 32:127 (2007)
152. Piarulli M, et al. *Phys. Rev. C* 91:024003 (2015)
153. Furnstahl RJ, Klco N, Phillips DR, Wesolowski S. *Phys. Rev. C* 92:024005 (2015)
154. Kölling S, Epelbaum E, Krebs H, Meißner UG. *Phys. Rev. C* 80:045502 (2009)